Enhancing the intergranular corrosion resistance and mechanical properties of Al–Mg–xSi–Cu–Zn alloys by synergistic intergranular and intragranular precipitation behaviors

Zhu, Liang; Guo, Mingxing; Li, Gaojie; Zhang, Jishan

DOI
10.1007/s10853-022-07527-8

Publication date
2022

Document Version
Final published version

Published in
Journal of Materials Science

J Mater Sci (2022) 57:14490–14510

Metals & corrosion

Enhancing the intergranular corrosion resistance and mechanical properties of Al–Mg–xSi–Cu–Zn alloys by synergistic intergranular and intragranular precipitation behaviors

Liang Zhu[1], Mingxing Guo[1,2,*], Gaojie Li[3], and Jishan Zhang[1,2,*]

[1] State Key Laboratory for Advanced Metals and Materials, University of Science and Technology Beijing, Beijing 100083, China
[2] Beijing Laboratory of Metallic Materials and Processing for Modern Transportation, University of Science and Technology Beijing, Beijing 10083, China
[3] Department of Materials Science and Engineering, Delft University of Technology, 2628 CD Delft, The Netherlands

Received: 14 June 2022
Accepted: 9 July 2022
Published online: 29 July 2022

ABSTRACT

The intergranular corrosion (IGC) resistance of age-hardening Al–Mg–Si–Cu alloys is closely related to the precipitation behavior adjacent to grain boundaries. In this study, we proposed to regulate the interaction of solute atoms and solute partitioning of Zn-containing Al–Mg–xSi–Cu alloys by introducing dislocations, which can synergistically decorate the intergranular and intragranular precipitation behavior. Consequently, the continuity of grain boundary precipitates and width of solute-depleted precipitate-free zones are inhibited accompanied with high number density or coarse precipitate in the matrix. As a result, the IGC resistance is greatly improved without strength and ductility loss, and the related mechanism has been proposed.

Introduction

Given the complexity of the material service environment, excellent comprehensive performance is the main goal for current material development. Owing to the combination of lightweight, high strength, good formability, and weldability, Al–Mg–Si alloys have been widely used in automotive, aerospace, marine, and construction fields [1, 2]. Although the corrosion resistance of Al–Mg–Si alloys is always acceptable, the intergranular corrosion (IGC) susceptibility of Al–Mg–Si alloys is inevitable after certain types of elemental additions (such as Cu, Zn, and excess Si) or aging treatment to improve their mechanical properties [3–5]. Therefore, it is of great significance to improve the corrosion resistance as well as mechanical properties of Al–Mg–Si–(Cu) alloys.

Handling Editor: Naiqin Zhao.

Address correspondence to E-mail: mingxingguo@skl.ustb.edu.cn; zhangjs@skl.ustb.edu.cn

https://doi.org/10.1007/s10853-022-07527-8

Numerous studies have demonstrated that Al–Mg–Si alloys are highly susceptible to IGC in the under-aged (UA state) or peak-aged (T6 state) state, while the dominant mode of corrosion in the overaged state (OA state) becomes extensive pitting corrosion [5–8]. In particular, Al–Mg–Si–(Cu) alloys gain the highest strength in the T6 state but are highly susceptible to IGC, which is associated with the formation of continuous electrochemical micro-couplings, consisting of the matrix, grain boundary precipitates (GBPs), and solute-depleted precipitate-free zones (PFZs) along grain boundaries [5–7, 9]. For improving the strength, it has been proposed that the addition of Cu to Al–Mg–Si alloys can substantially improve the strength, but deteriorate the IGC resistance due to the formation of a cathodic Cu-enriched film, Q phase ($Al_4Mg_8Si_7Cu_2$) and its precursors at grain boundaries [9–11]. And Zou et al. [11] proposed that the deterioration effect of Cu content on the IGC resistance of Al–Mg–Si alloys is improved by adding excess Mg due to the formation of discontinuous Q' precipitates ($Al_3Mg_9Si_7Cu_2$) on the grain boundaries. However, the role of Mg and Si elements in Al–Mg–Si alloys is mutually exclusive, where excess Mg is detrimental to strength and ductility. Accordingly, excess Si is usually added to improve the strength and ductility of Al–Mg–Si alloys [12–14], but Si content may preferentially segregate at the grain boundaries, which in turn increases the IGC susceptibility [10, 15, 16]. In recent years, numerous studies have also found that Zn addition gives a significant effect on age-hardening response, peak-aging strength, and IGC susceptibility of Al–Mg–Si–Cu alloys [17–19]. When the Zn content is lower than 1.0 wt%, Zn addition leads to a high IGC susceptibility due to the formation of a continuous thin film caused by the segregation of Zn at the grain boundaries, and the IGC susceptibility increases with Zn content due to the increase in the corrosion potential difference between the PFZs and GBPs caused by the coarsening of GBPs [20, 21]. However, when the Zn concentration is 2.0 to 4.0 wt%, Mg–Zn and Zn-containing Mg–Si precipitates are formed along the grain boundaries to replace the Cu-rich precipitates, which in turn reduces the corrosion potential difference between the PFZs and Al matrix. Meanwhile, the size of GBPs and width of PFZs in the T6 state also decrease when the Zn content exceeds 2.0 wt%. Accordingly, the IGC resistance can be enhanced and increased by increasing Zn content containing (2.0–4.0 wt%) Al–Mg–Si–Cu alloys [20]. In short, the intragranular and intergranular (GBPs, Cu/Zn-rich films, and PFZs) precipitation behavior of Al–Mg–Si–Cu–Zn alloys can be regulated synergistically by the complex interaction of Mg, Si, Cu, and Zn.

Furthermore, to improve the IGC resistance of Al–Mg–Si–(Cu) alloys without mechanical properties loss, extensive aging treatment processes, including aging time and aging temperature, have been widely studied. Typically, overaging treatments are often used to inhibit the IGC susceptibility of Al–Mg–Si–(Cu) alloys, but with a small loss of strength. Subsequently, Wang et al. [22] proposed that a two-step overaging treatment (180 °C/2 h + 160 °C/120 h) designated as the T78 temper can improve the IGC resistance of 6056 alloys without strength loss due to the formation of discretely distributed GBPs in grain boundaries with the high number density of β'' precipitates in the matrix. And Li et al. [8] designed a novel thermomechanical treatment consisting of pre-aging, cold-rolling, and re-aging to simultaneously enhance the tensile properties and IGC resistance of Al–Mg–Si–(Cu) alloys by forming small-angle grain boundaries, discontinuous distribution of GBPs, and sufficient precipitation of the matrix solutes during the thermomechanical treatment. Furthermore, Xu et al. [23] also reported that the IGC resistance of Al–Mg–Si alloys with low Zn content can be enhanced by the interrupted aging treatment (T6I6) due to the formation of small and discretely distributed GBPs, narrower PFZs, and fine, densely distributed intragranular precipitates (IPs). However, all these processes are more complex and narrowly applicable in the actual industry.

Here, it has been found that dislocations introduced by pre-deformation can provide heterogeneous nucleation sites for IPs (GP zones, β'' phase) and act as short-circuit diffusion paths for solute atoms to accelerate the nucleation and growth of IPs in Al–Mg–Si–(Cu) alloys during the aging process, which can increase the strength and age-hardening response [24–27]. However, it has been proposed that corrosion susceptibility of steels increases with increasing deformation due to the formation of less compact and thin oxide films and a negative offset in pitting potential [28, 29]. In addition, various studies have also shown that the pitting and IGC susceptibility of aluminum alloys increases with the introduction of pre-deformation treatment due to the distribution of residual strain across grains [30–33].

However, for Al–Mg–Si–Cu–Zn alloys, Zn addition strongly affects the nucleation and growth of both the GBPs and IPs due to the highest diffusion rate, their similar atomic radius and electronegativity of Zn to Al [20, 21]. The nucleation of intragranular precipitates and intergranular precipitates is always mutually exclusive, which can be amplified with the introduction of dislocation. Simultaneously, solute atoms may also preferentially segregate along dislocations induced by pre-deformation treatment, while the concentration of solute atoms in the matrix decreased, thus affecting the intergranular precipitation behavior of Al–Mg–Si–(Cu) alloys. Furthermore, although the IGC susceptibility of Al–Mg–Si alloys increases with the increased Si content, the strength and age-hardening rate can be enhanced by Si content, which can synergistically regulate the intragranular and intergranular precipitation behavior [34].

Therefore, in the present study, we propose to systematically study the synergistic effect of intragranular/intergranular precipitation and corrosion behaviors of Al–Mg–Si–Cu alloys with low Zn content by coupling pre-deformation treatment and Si content and provide new insight for improving both the mechanical properties and intergranular corrosion.

Experimental

Three Al–Mg–Si–Cu–Zn alloys were casted and rolled into a thickness of 1.0 mm, as shown in Ref.[34], and their compositions are listed in Table 1. In the peak-aged state, the main strengthening precipitates of Al–Mg–Si alloys are β'' phases. Many studies [35–37] proposed that the composition of the β'' phase is $Mg_{(5-x)}Al_{(2+x)}Si_{4(x\approx 1)}$ due to the substitution of Al atoms for Mg or Si atoms in the Al–Mg–Si alloys. Moreover, Si3/Al sites of the β'' phase sometimes can be replaced by Zn atoms in the Zn-containing Al–Mg–Si alloys [19]. Therefore, an Al–Mg–Si–Cu–Zn alloy with an Mg/Si atomic ratio of less than 1.25 can be defined as an alloy with excess Si content in this study. Then, the final cold-rolled alloy sheets were solution treated in a salt bath furnace at 555 °C for 2 min, followed by quenching in water at room temperature (20 °C). Solution-treated alloy sheets were directly pre-aged through cooling from 80 to 40 °C within 12 h (PA state). Finally, pre-aged samples were pre-deformed to 0, 2, and 8% by tensile test, followed by isothermal aging at 185 °C.

The micro-hardness of the aged alloy sheets was measured using a 401 type MVD Vickers hardness (HV) tester with a load of 1.96 N and a loading time of 15 s. Five hardness indentations were measured on each sample, and the average hardness was reported. Samples for micro-hardness measurements were prepared by mechanical grinding and polishing to a final SiO_2 suspension (1.0 μm) finish. Tensile tests were conducted on a Mechanical Testing and Simulation (MTS) 810 machine with a strain rate of 1×10^{-3} at room temperature. Tensile samples with a gauge length of 50 mm and cross section of 12.5 × 1.0 mm were mechanical ground on SiC papers from 400 to 2000 grit size.

The IGC susceptibility was evaluated according to the ASTM G110 standard. The corrosion test sample with a size of 20 (length) × 12.5 (width) × 1 mm(thickness) was mechanically ground on SiC papers from 400 to 2000 grit size, and its length direction was parallel to the rolling direction of the sheets (as shown in Fig. 1). All the samples were degreased in acetone, and then, they were etched for 60 s in an etching cleaner (5 mL hydrofluoric acid (HF, 48%) and 50 mL nitric acid (HNO_3, 70%) per liter of deionized water) at 93 °C. Subsequently, the etched samples were immersed in concentrated nitric acid (70%) for 60 s and rinsed in reagent water and air-dried. Finally, the etched samples were further immersed in a solution of 10 mL hydrogen peroxide (H_2O_2, 30%) and 57 g sodium chloride (NaCl) per liter of deionized water at 30 °C for 24 h. Afterward, each corroded sample was cut along the dashed line as shown in Fig. 1, which is an interval normal to its rolling direction.

Table 1 The composition of the experimental alloys (wt%)

Alloy	Al	Si	Mg	Cu	Zn	Mn	Fe	Ti	Ni	Mg/Si
A	Bal	0.55	0.70	0.20	0.52	0.15	0.20	0.02	0.01	1.43
B	Bal	0.76	0.70	0.20	0.54	0.15	0.20	0.02	0.01	1.04
C	Bal	1.08	0.67	0.19	0.53	0.15	0.20	0.02	0.01	0.72

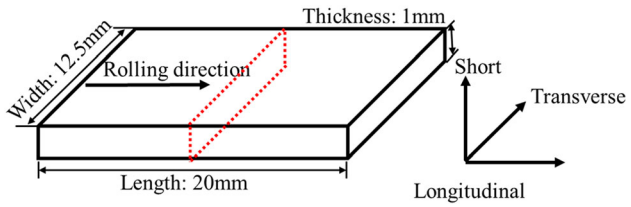

Figure 1 Schematic diagram of the corrosion test sample.

The obtained short transverse (S-T) cross sections were mechanical ground and polished to a final SiO_2 suspension (1.0 μm) finish. The corroded samples' depths and grain corrosion morphology were assessed by examining S-T cross sections using a Carl Zeiss Axio Imager A2m optical microscope (OM).

Electrochemical corrosion testing of the different samples was conducted on a CHI660D electrochemical workstation. The potentiodynamic method was performed on a three-electrode cell with platinum as the counter electrode, a saturated calomel reference electrode (SCE) as the reference electrode, and the sample as a working electrode with an exposed area of 100 mm^2. Before testing, the electrochemical corrosion testing samples were first ground and polished. The open circuit potential (OCP) was recorded in a 3.5 wt% NaCl solution for 1200 s to ensure a stable state prior to the polarization testes. The potentiodynamic polarization curves were scanned from − 1200 to − 200 mV with a scanning rate of 0.5 mV/s.

The crystal structure, morphology, distribution, and orientation of the precipitates and grain boundary dispersion phases were characterized by a TecnaiG2 F30 high-resolution transmission electron microscopy (HRTEM) equipped with X-ray energy-dispersive spectrometer (EDS) systems and a high angle annular dark-field scanning transmission electron microscopy (HAADF-STEM) detector at 300 kV, and the fast Fourier transform (FFT) images of typical precipitates were reconstructed by Digital Micrograph Software. Samples for TEM studies were prepared by twin-jet polished in a solution of 30 vol% nitric acid and 70 vol% methanol at − 20 ∼ − 30 °C.

Results

Age-hardening behavior and mechanical properties

Figure 2 shows the micro-hardness for the pre-aged alloys with the different pre-deformation ratios as a function of aging time at 185 °C. As expected, the hardness first increases up to a peak value and then decreases with time, showing the typical age-hardening behavior of Al–Mg–Si alloys, which mainly contain three stages consisting of underaged state (UA), peak-aged state (T6), and overaged state (OA) [17, 20, 38]. The peak hardness value of the alloys increases as Si content increases, but is independent of the pre-deformation ratio. However, the time to reach the T6 state is significantly reduced by pre-deformation treatment and also decreases as the pre-deformation ratio increases (the circle in Fig. 2).

The corresponding tensile mechanical properties of the different samples in the T6 state are shown in Fig. 3. In the T6 state, the yield strength increases as Si content increases, whereas the pre-deformation treatment has little effect on the strength of the alloys. These results are consistent with the hardness results in Fig. 2. Furthermore, the elongation of the peak-aged alloys decreases slightly as the pre-deformation ratio increases, but is still close to 10%. In brief, pre-deformation treatment has little effect on the strength and elongation of the peak-aged alloys, but can accelerate the age-hardening rate, which associates with the nucleation and growth rate of precipitates.

Corrosion behavior

Figure 4 shows the typical cross-sectional (S-T) corrosion morphologies with the different pre-deformation ratios in the T6 state, and the corresponding maximum IGC depths are summarized in Fig. 5. In the T6 state, the IGC depth of the undeformed alloy first increases and then remains almost constant with the increased Si content. On the other hand, the depth of the three alloys changes with the pre-deformation ratio, but does not continuously decrease with the increase of the pre-deformation ratio. In most cases, the IGC depth of the pre-deformed alloys decreases compared to the undeformed alloys, while the IGC depth of alloy A with 2% PD increases instead. For the pre-deformed alloys, with an increasing pre-deformation ratio, the IGC depth of alloys A and C

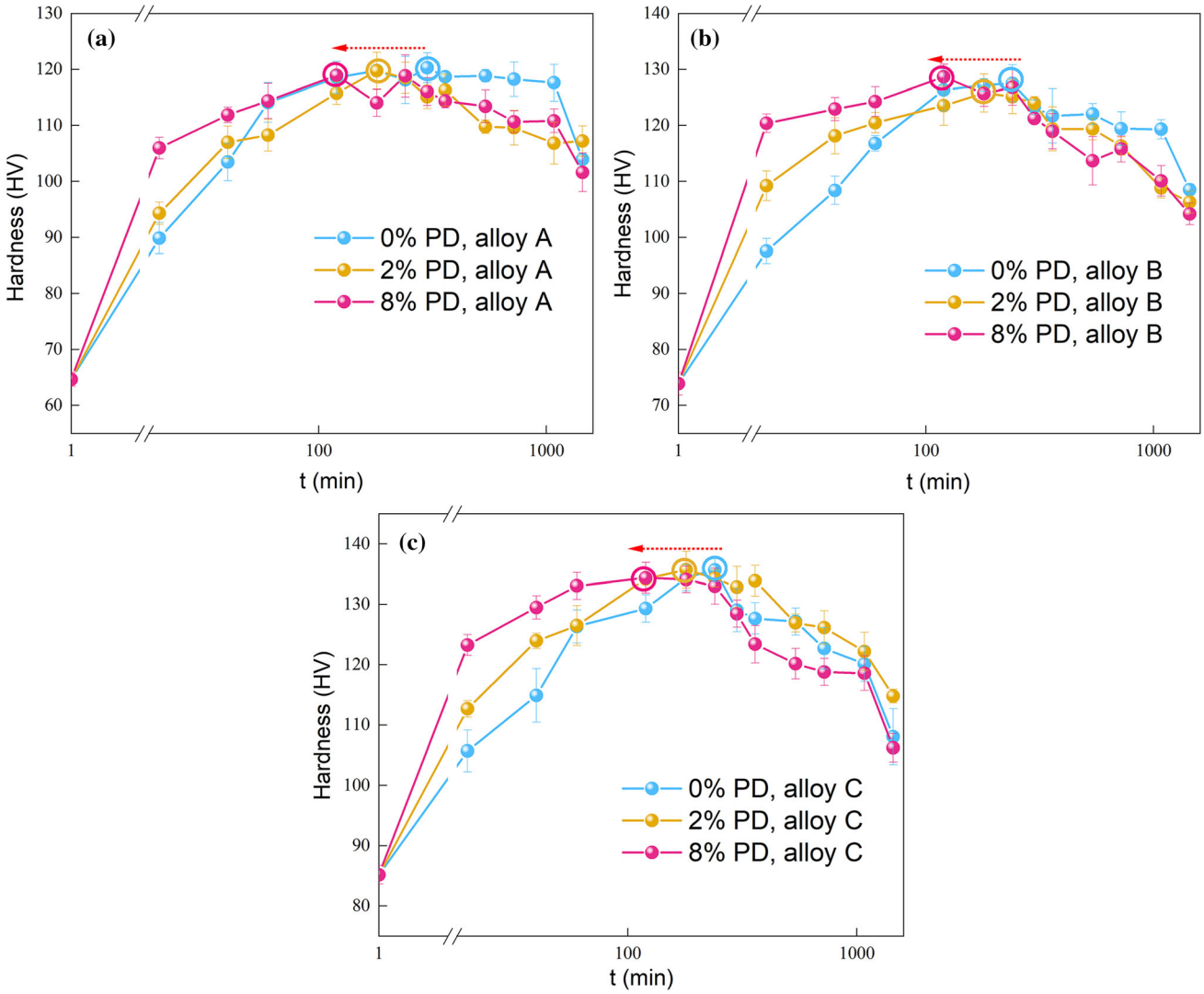

Figure 2 Variations of hardness for the pre-aged alloys with different pre-deformation (PD) ratios at 185 °C. **a** alloy A, **b** alloy B, **c** alloy C.

gradually decreases, while the IGC depth of alloy B first increases and then decreases. In short, the IGC resistance of the peak-aged alloys decreases with excess Si addition but can be generally improved by pre-deformation treatment. However, the excellent IGC resistance is also related to the coordinated combination of Si content and pre-deformation ratio, which is strongly affected by the intergranular and intragranular precipitate behaviors.

The potentiodynamic polarization curves of the three alloys with the different pre-deformation ratios in the T6 state are shown in Fig. 6. All the curves show that the current density sharply increased at an approximate corrosion potential (E_{corr}), indicating that the corrosion potential (E_{corr}) coincided with the pitting potential (E_{pit}). The symmetry of the anodic polarization and cathodic polarization curves is relatively low, while some anodic polarization curves have obvious strong polarization areas. Therefore, it is suitable to use the cathodic polarization curve extrapolation method to calculate the values of corrosion current density (I_{corr}) [39]. Herein, the values of E_{corr} and I_{corr} were derived from the potentiodynamic polarization curves by Tafel fitting as shown in Table 2. For undeformed alloys, with the increased Si content, the I_{corr} value increases, and the E_{corr} value first increases slightly and then decreases, giving rise to the decreasing order of corrosion resistance: alloy A > alloy B > alloy C. For pre-deformed alloys, both the E_{corr} and I_{corr} values do not continuously decrease

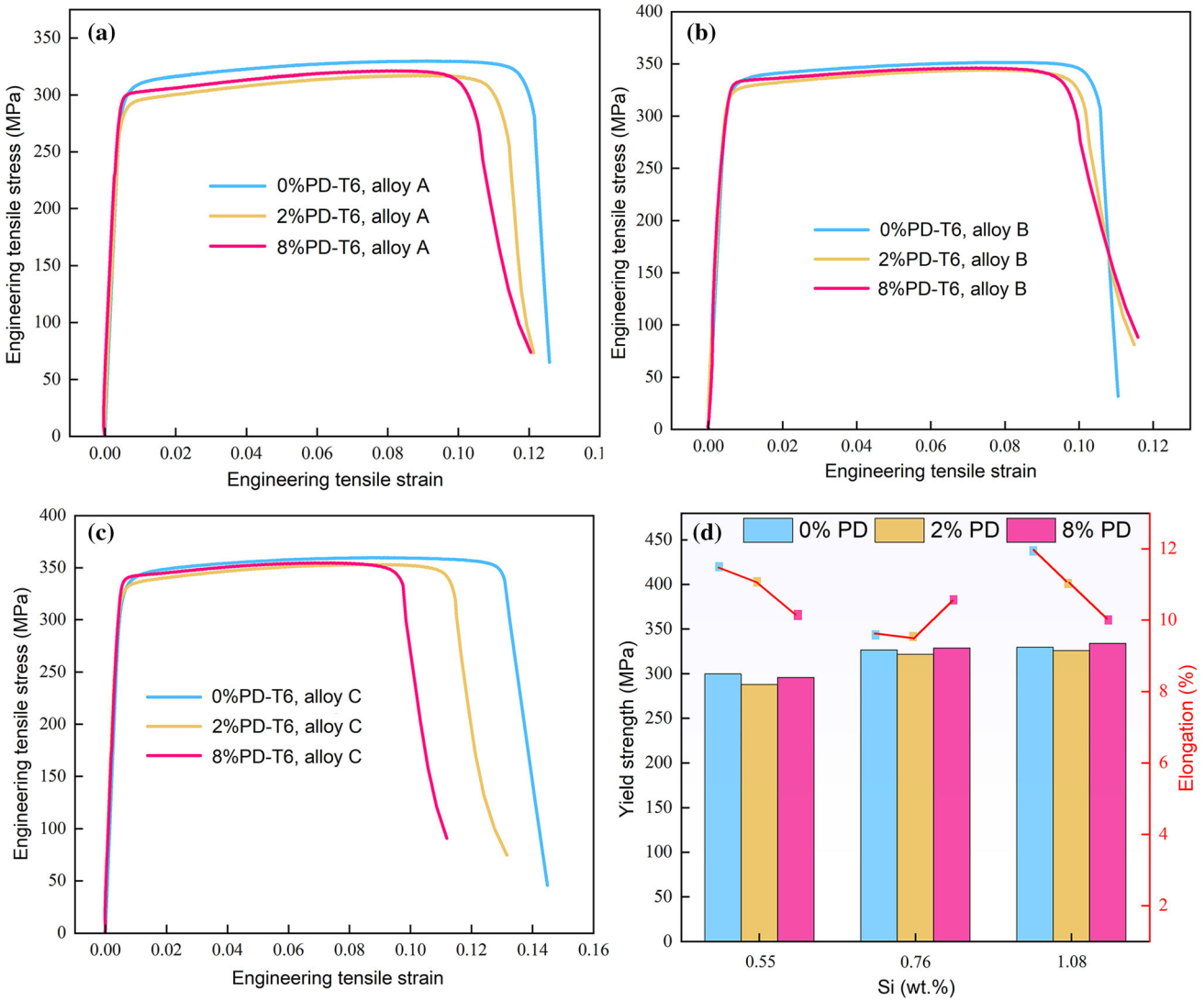

Figure 3 Mechanical properties of the alloys with different pre-deformation (PD) ratios in the peak-aging state (T6). **a** alloy A, **b** alloy B, **c** alloy C, **d** yield strength and elongation.

with increasing pre-deformation ratio, but also depend on the Si content. With an increasing pre-deformation ratio, both the E_{corr} and I_{corr} values in alloy A first increase and then decrease; however, the changing trend of the I_{corr} value in alloys B and C is the opposite. Additionally, the E_{corr} values in alloys B and C slightly change with the change in pre-deformation ratio, because the corrosion potentials of the Al alloys depend mainly on the solute concentrations in the solid solution and are less sensitive to the second phase particles and grain boundaries [40]. It can be inferred that pre-deformation treatment and Si content significantly change the corrosion kinetics of Al–Mg–Si–Cu–Zn alloys, which is related not only to the volume fraction of precipitates in the grain boundaries but also to the distribution and composition of the precipitates and PFZs. Although the decrease in the I_{corr} value is always related to the decrease in the volume fraction of the precipitates, it is unclear whether the change in the E_{corr} and I_{corr} values are controlled by cathodic or anodic kinetics [20]. Furthermore, pre-deformation treatment and Si content can enhance the age-hardening response, whereas the yield strength can also be improved by Si content. Accordingly, an excellent comprehensive performance (age-hardening rate, strength, and IGC resistance) can be achieved simultaneously in Al–Mg–Si–Cu–Zn alloys by coupling the pre-deformation ratio and Si content. Considering the different corrosion behaviors and strengths of the three alloys

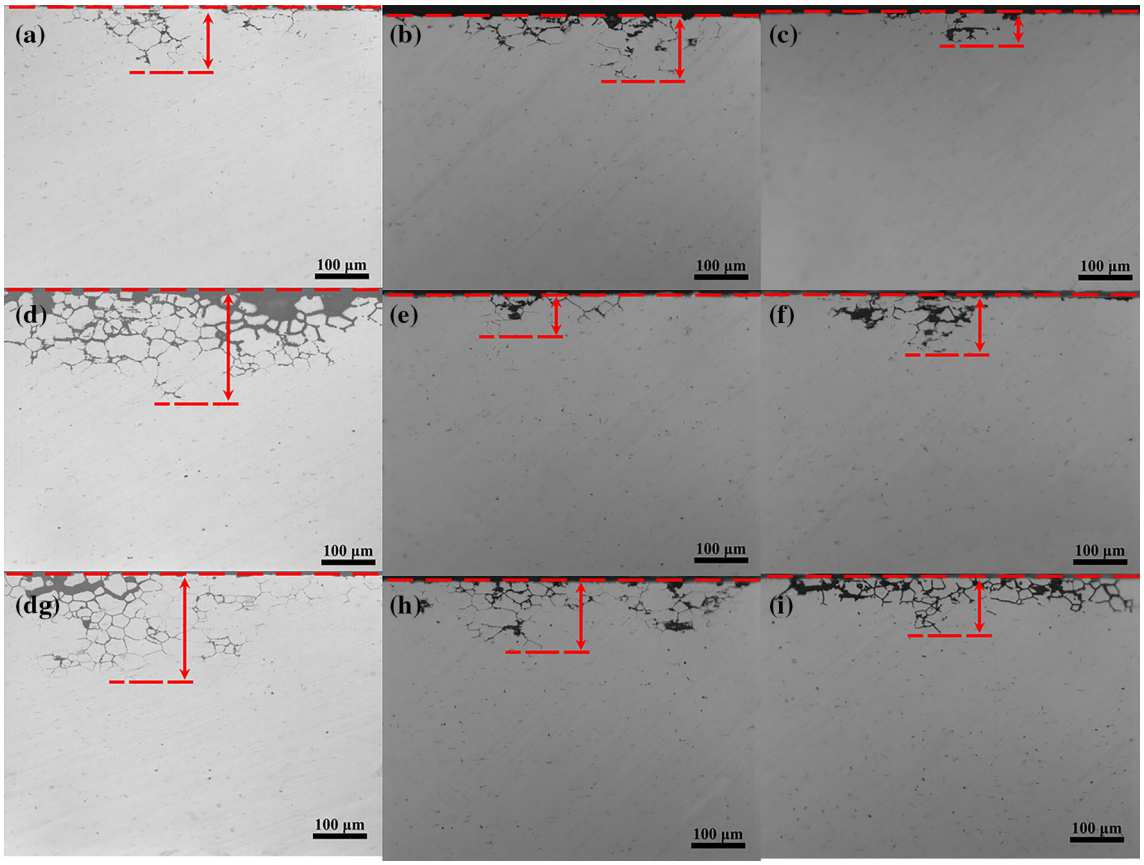

Figure 4 Typical cross-sectional (S-T) intergranular corrosion morphologies of the alloys with different pre-deformation ratios in the peak aged state. **a-c** alloy A: 0, 2 and 8% PD, respectively. **d-f** alloy B: 0, 2 and 8% PD, respectively. **g-i** alloy C: 0, 2 and 8% PD, respectively.

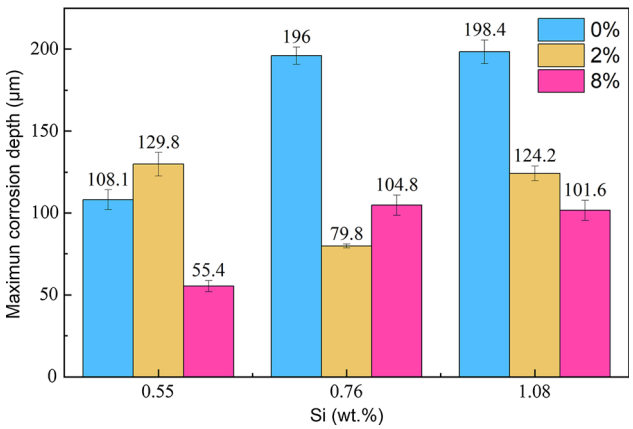

Figure 5 Statistical diagram of the maximum corrosion depths of the alloys with different pre-deformation ratios in the peak aged state.

in the T6 state, the distribution of intergranular and intragranular precipitates needs to be further analyzed.

Microstructure characterization

Figure 7 shows the intragranular precipitates of the three alloy sheets with the different pre-deformation ratios in the T6 state, and the corresponding HRTEM images of typical precipitates are shown in Fig. 8. For undeformed alloys (Fig. 7a, d, and g), many needle-shaped precipitates are uniformly distributed in the matrix, and their average length increases as Si content increases. According to the HRTEM analysis, two typical precipitates can be found, including the β″ phase and pre-Q′ phase (Fig. 8a, b). For the pre-deformed alloys, precipitates tend to nucleate along dislocations. According to the HRTEM analysis (Fig. 8), the precipitates in the matrix of no dislocation are still spherical and can be identified as the β'' phase and GP zone, while the precipitate along the dislocation is rectangular and can be recognized as polycrystalline B′/U2 precipitates (MgAlSi, Mg/Si ~ 1) or Q' precipitates [26]. Due to the existence of various types of precipitates along < 001 > Al, we

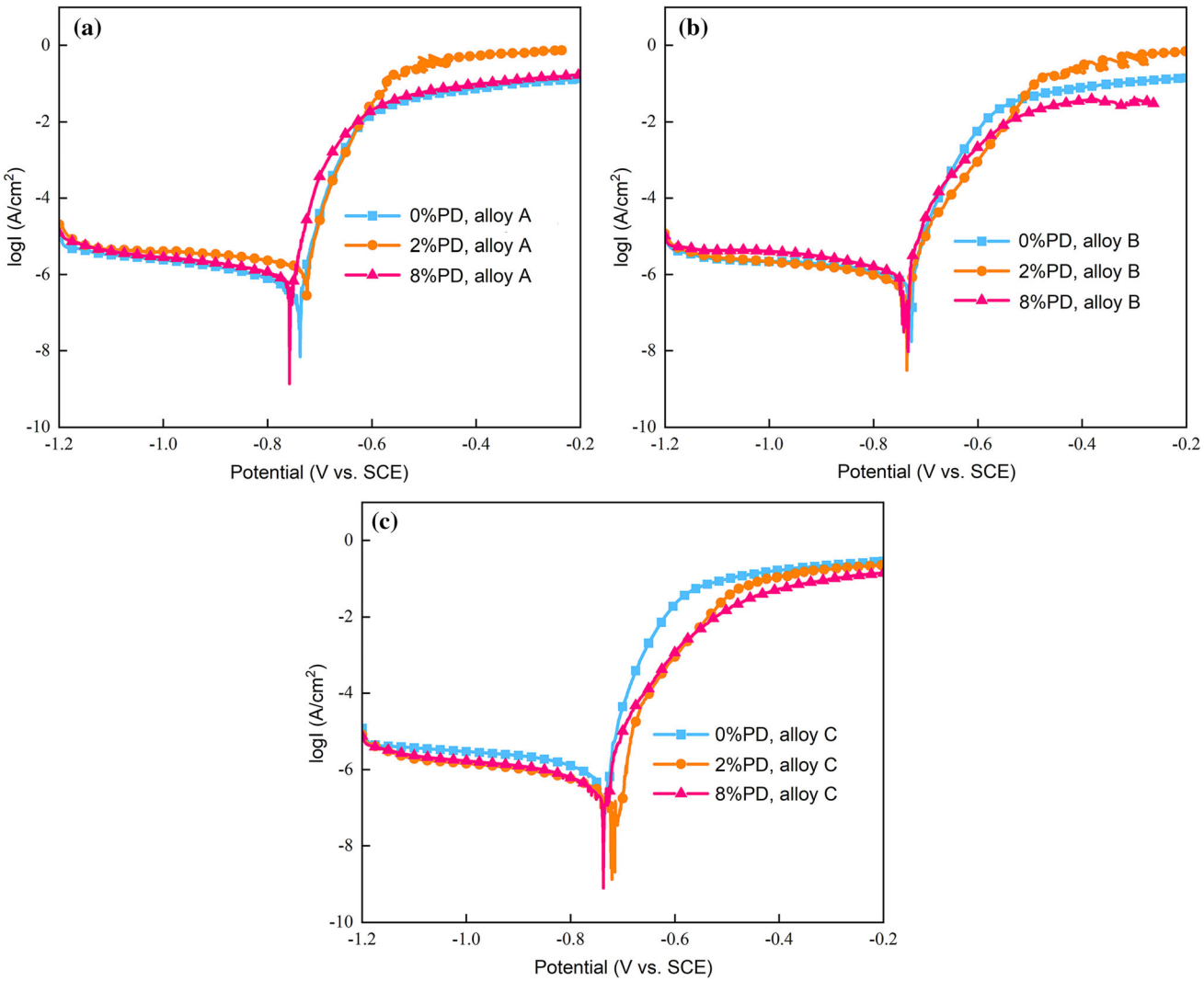

Figure 6 Potentiodynamic polarization curves in deaerated 3.5 wt% NaCl solution for the alloys with various pre-deformation ratios in the peak aged state. **a** alloy A, **b** alloy B, **c** alloy C.

Table 2 Corrosion related parameters in 3.5 wt% NaCl for the experimental alloys under the different conditions

Condition	Corrosion potential E_{corr} versus SCE (V)	Corrosion current density I_{corr} (μA/cm^2)
0%PD, alloy A	− 0.737	0.335
2%PD, alloy A	− 0.731	1.439
8%PD, alloy A	− 0.759	0.731
0%PD, alloy B	− 0.727	0.530
2%PD, alloy B	− 0.736	0.437
8%PD, alloy B	− 0.741	0.785
0%PD, alloy C	− 0.744	0.728
2%PD, alloy C	− 0.725	0.216
8%PD, alloy C	− 0.738	0.272

have calculated the areal number density (Na) and average length (l) of precipitates based on TEM and HRTEM images, as shown in Table 3. It is clear that the number density of precipitates in the alloys with 2% PD is significantly higher than that in the undeformed alloys and also increases as Si content

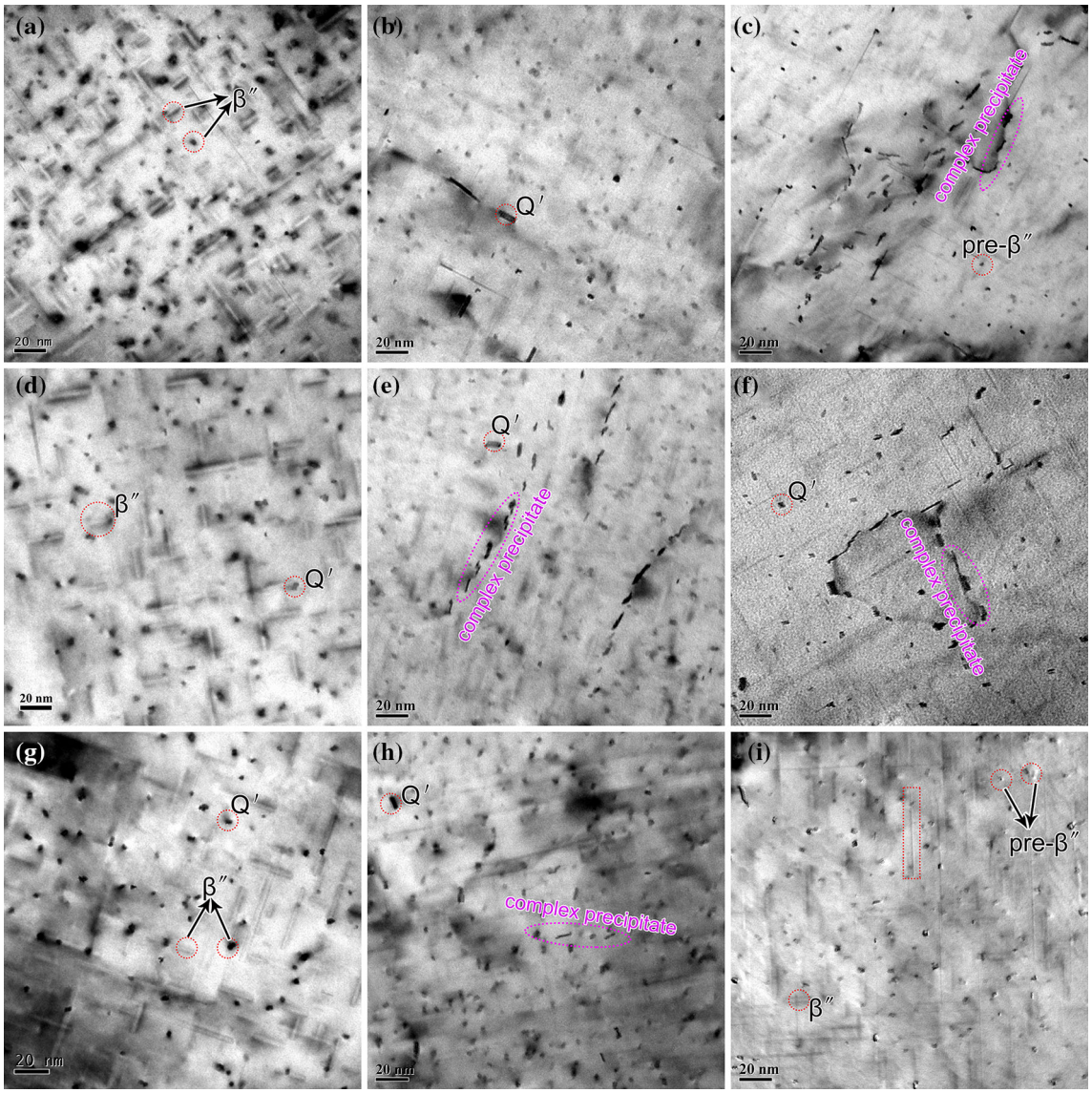

Figure 7 TEM bright field images of the three alloy sheets with different pre-deformation (PD) ratios in the peak aged condition. **a**–**c** alloy A: 0%, 2% and 8% PD, respectively, **d**–**f** alloy B: 0%, 2% and 8% PD, respectively, **g**–**i** alloy C: 0%, 2% and 8% PD, respectively.

increases, indicating that the nucleation rate of intragranular precipitates can be greatly enhanced by coupling pre-deformation and Si content. With a further increase in the pre-deformation ratio to 8%, more precipitates preferentially nucleate and grow along the dislocations, whereas the number density of precipitates in the matrix of no dislocations decreases. Accordingly, the number density of intragranular precipitates of the three alloys all decreases after 8% PD due to a limited nucleation rate of precipitates in the matrix of no dislocations. Additionally, the radius of precipitates decreases, but the average length of those precipitates increases with different pre-deformation ratios and Si content.

The distribution, morphology, and precipitation kinetics of intragranular precipitates can be largely affected by the introduction of dislocations, while the intergranular precipitation behavior is strongly associated with the intragranular precipitation behavior, which further influences the IGC susceptibility. As a result, HAADF-STEM images of GBPs in the peak-aged alloy with the different pre-deformation ratios are shown in Fig. 9. It can be found that the areal number density of GBPs in the undeformed

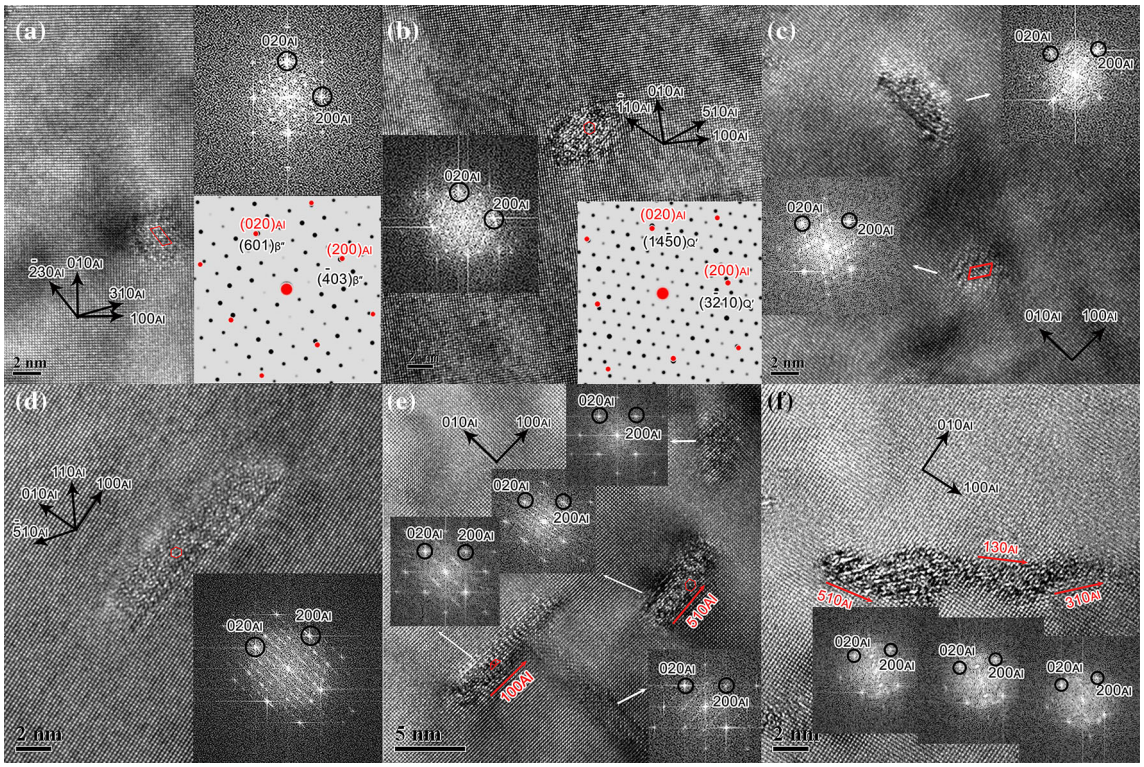

Figure 8 HRTEM and FFT images of the typical precipitates in the peak aged condition. **a** β″ in Fig. 7a; **b** Q′ in Fig. 7d; **c** β″ and pre-β″ in Fig. 7i; **d** Q′ in Fig. 7f; **e** complex precipitates in Fig. 7e; **f** complex precipitates in Fig. 7f.

Table 3 The areal number density (*Na*) and average length (*l*) of precipitates in the peak-aged state.

Condition	Na/10^{15} m^{-2}	l/nm
0%PD, alloy A	1.79 ± 0.06	14.8 ± 0.3
2%PD, alloy A	2.52 ± 0.24	18.0 ± 1.2
8%PD, alloy A	2.06 ± 0.14	33.2 ± 2.5
0%PD, alloy B	1.45 ± 0.09	19.7 ± 0.3
2%PD, alloy B	3.25 ± 0.25	19.8 ± 1.8
8%PD, alloy B	1.55 ± 0.03	42.0 ± 5.4
0%PD, alloy C	1.29 ± 0.10	23.6 ± 0.9
2%PD, alloy C	3.63 ± 0.18	20.9 ± 1.5
8%PD, alloy C	1.07 ± 0.03	43.0 ± 4.3

PD pre-deformation

alloys A, B, and C are $(2.13 \pm 0.23) \times 10^{12}$, $(4.27 \pm 0.51) \times 10^{12}$, and $(5.33 \pm 1.1) \times 10^{12}$ m^{-2}, respectively. The number density of GBPs increases as Si content increases in the undeformed alloys, giving rise to a higher IGC susceptibility. Hereafter, the number density of GBPs decreases significantly in the three alloys after pre-deformation treatment, except for alloy A with 2% PD. As a result, the continuity of GBPs is decreased by pre-deformation. It can be inferred that dislocation introduced by pre-deformation improves the intragranular precipitation kinetics but suppresses the grain boundary precipitation kinetics in the three alloys. However, the number density of GBPs increases and the distribution is more continuous in alloy A with 2% PD, indicating that the grain boundary precipitation kinetics are also associated with the segregation of solute atoms.

Accordingly, the element line scanning analysis of grain boundaries was carried out by EDS, and the results for selected typical precipitates are shown in Fig. 10. According to the element line scanning analysis, the observed GBPs in the undeformed alloys contain Al, Mg, Si, Cu, and Zn elements, whereas the GBPs in the pre-deformed alloys mainly contains Al, Mg, and Si elements, indicating that the segregation of Cu and Zn elements has been suppressed. Additionally, pure Si particles can be formed in alloy C (Si-rich alloys) with pre-deformation treatment. Therefore, it can be inferred that the formation of Cu-rich film or Zn-rich film along grain boundaries may be inhibited by pre-deformation treatment, which is

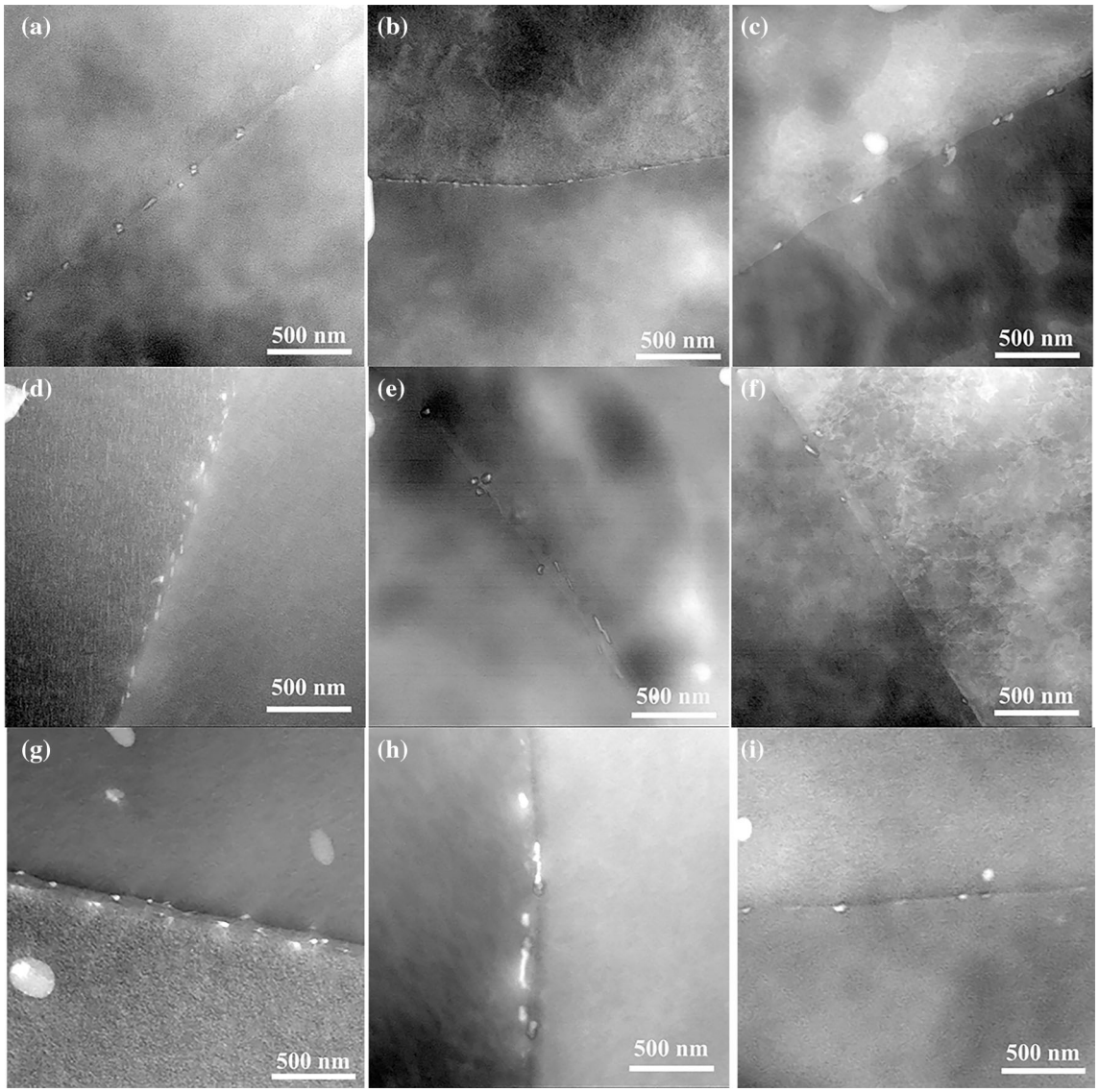

Figure 9 HAADF-STEM images of grain boundary precipitates in the three alloy sheets with different pre-deformation (PD) ratios in the peak aged condition. **a**–**c** alloy A: 0, 2 and 8% PD, respectively, **d**–**f** alloy B: 0, 2, and 8% PD, respectively, **g**-**i** alloy C: 0, 2, and 8% PD, respectively.

beneficial to improve the IGC resistance of Al–Mg–Si–Cu–Zn alloys. Simultaneously, the intragranular precipitation and grain boundary precipitation kinetics will also influence the formation of PFZs.

Subsequently, typical bright-field TEM images of the grain boundary regions of the three alloys with different pre-deformation ratios in the T6 state are shown in Fig. 11. Herein, one grain adjacent to the grain boundaries is adjusted to be parallel to the $[001]_{Al}$ zone axis to characterize the variation of the widths of PFZs, but the another adjacent grain is not parallel to [001] Al zone axis, so the observed width of PFZs is half of the actual width. Consequently, the widths of PFZs of the undeformed alloys A, B, and C are 160, 208.8, and 221.2 nm, respectively, showing an increasing trend upon the increased Si content. For the pre-deformed alloys, the widths of PFZs gradually decrease or even disappear, while some nano-precipitates even precipitate along the grain boundaries. Concretely speaking, although the width of the PFZs in alloy A decreases with the increasing pre-deformation ratio, there is still a certain width. The widths of PFZs gradually disappear in alloy B and alloy C with 8% PD, indicating that the formation of PFZs is closely related to both the pre-deformation ratio and Si content.

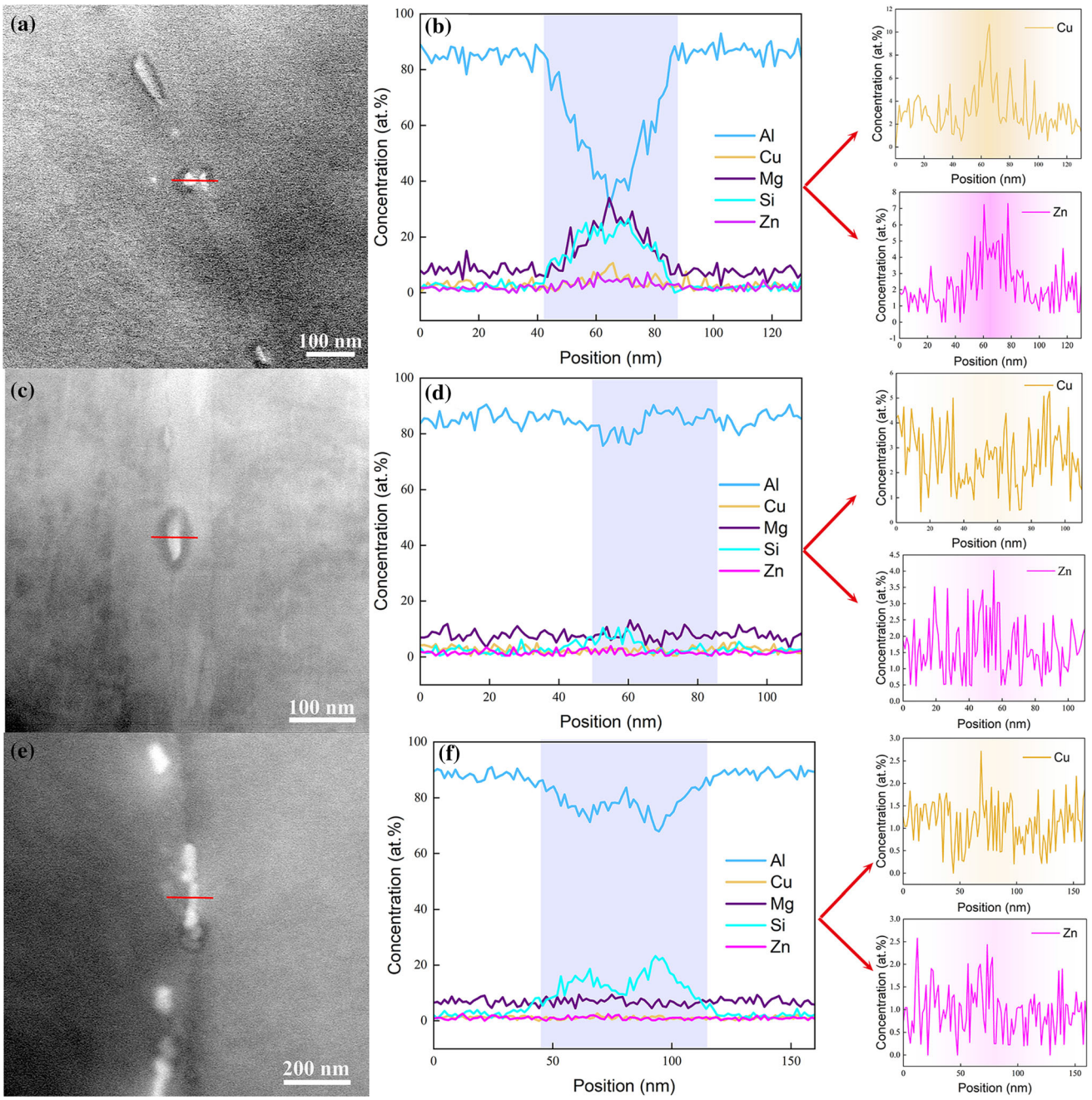

Figure 10 Intergranular STEM-HAADF images and element line scanning on the grain boundary precipitates under typical conditions. **a**, **b** alloy A without pre-deformation (PD); **c**, **d** alloy B with 8% PD; **e**, **f** alloy C with 2% PD.

Discussion

Intragranular precipitation behavior of Al–Mg–xSi–Cu–Zn alloys

After solution treatment, the growth and nucleation rate of precipitates (Mg–Si solute clusters, GP zones, or pre-β'' phase) in age-hardening Al–Mg–Si–(Cu) alloys are mainly controlled by the vacancy-assisted diffusion of solute atoms during the following aging process. Extensive studies have shown that many fine solute clusters can be formed during the pre-aging process, and Si can also promote the nucleation of stable Mg-Si solute clusters with the tendency of easily transforming into the β'' phase [14, 41]. Accordingly, more stable solute clusters can be

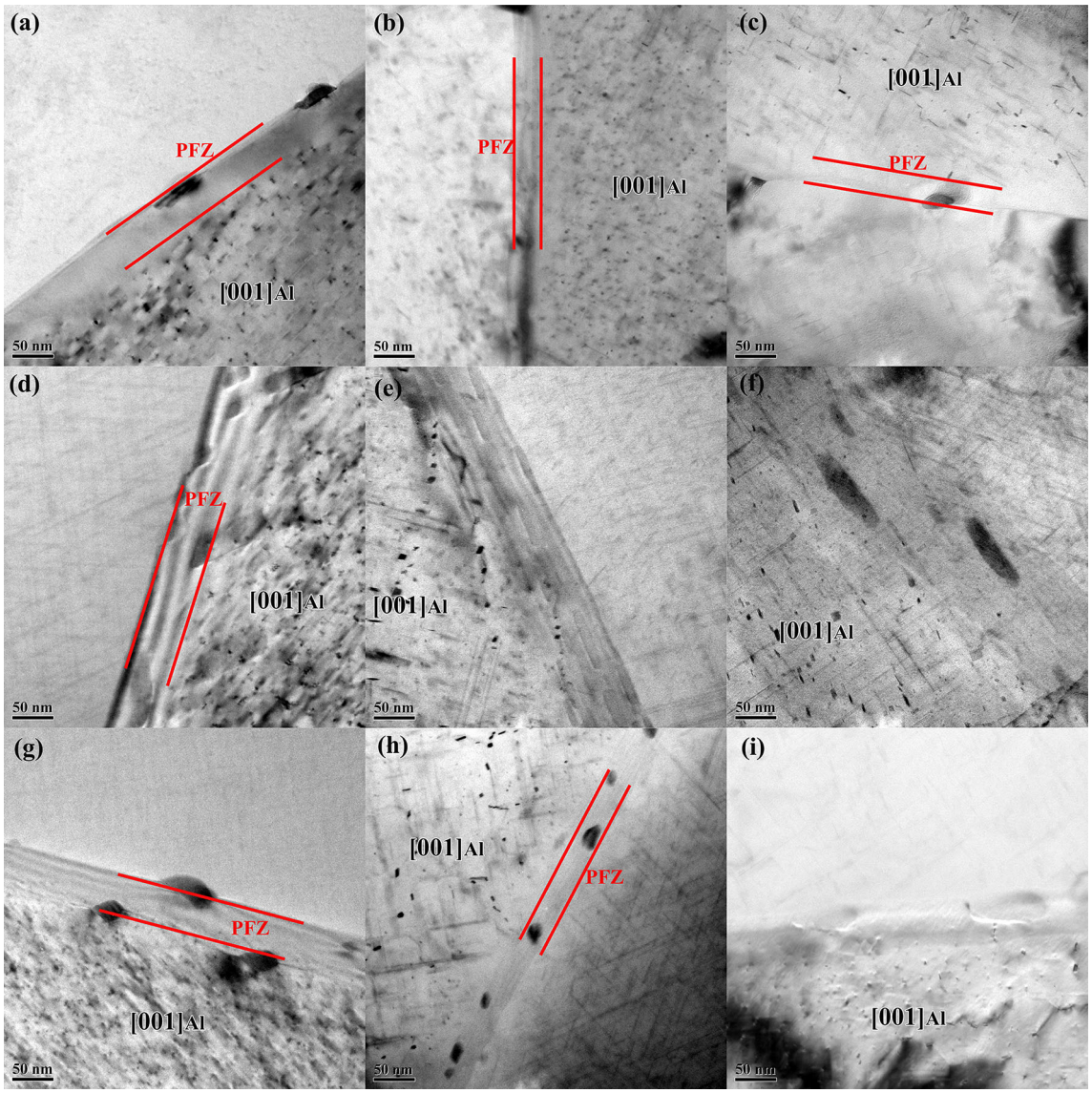

Figure 11 TEM images of grain boundaries in the three alloy sheets with different pre-deformation (PD) ratios in the peak aged condition. **a**–**c** alloy A: 0, 2, and 8% PD, respectively; **d**–**f** alloy B: 0, 2, and 8% PD, respectively; **g**–**i** alloy C: 0, 2, and 8% PD, respectively.

formed upon the increase of Si content in the Al–Mg–Si–Cu–Zn alloys during the low-temperature pre-aging process [42], and they can easily transform into the β'' phase during the isothermal aging process, thus leading to a higher average length of needle precipitates (β'' phase) in the T6 state (Fig. 7a, d, g). However, some new solute clusters can re-nucleate and grow during the isothermal aging process due to the dissolution of unstable solute clusters in Mg-rich alloys and the high temperature of isothermal aging, but the growth rate of those new β'' phases is limited due to the low concentration of Si contents and vacancies [34]. Therefore, the average length of needle precipitates (β'' phase) increases, but the number density slightly decreases with the increased Si content in the T6 state (Fig. 7a, d, g).

With the introduction of dislocations, the number density and morphology of intragranular precipitates changed significantly. On the one hand, dislocations always act as heterogeneous nucleation sites for precipitates in metal materials, and promote the diffusion of solute atoms. Therefore, some precipitates can preferentially precipitate along dislocations by heterogeneous nucleation mechanisms [27, 43–46]. On the other hand, previous studies indicated that solute clusters formed during pre-aging treatment

can grow into β'' phases while the size of solute clusters is larger than the critical value, otherwise they could be dissolved [47–51]. Here, the critical nucleation growth size of solute clusters can be reduced due to the increased total strain energy induced by pre-deformation [27, 52], leading to a higher homogeneous nucleation rate in the matrix of no dislocations. At the same time, the heterogeneous nucleation sites are limited due to the relatively low density of dislocations with 2% PD, so many precipitates can nucleate and grow in the matrix of no dislocations by the homogeneous nucleation mechanism during the isothermal aging process. Accordingly, the number density of precipitates (β″) in the peak-aged alloys can be increased by 2% PD due to the synergetic effect of the homogeneous/heterogeneous nucleation mechanism (Fig. 7b, e, h) [27].

Furthermore, the slip and multiplication of dislocations are always associated with the volume fraction and distribution of precipitates in metallic materials during plastic deformation [53–59]. For Fe-containing Al–Mg–Si–Cu–Zn alloys, there are mainly two types of precipitates in the pre-aged state, including non-shearable precipitates (Al(Fe,Mn)Si, Q) and shearable precipitates (solute-cluster, pre-β''). Our previous studies [12] demonstrated that non-shearable precipitates (Al(Fe,Mn)Si, Q) distributed more uniformly as Si content increased. Moreover, Si content can also promote the nucleation of shearable precipitates (solute-cluster, pre-β'') in the pre-aged Al–Mg–Si–Cu–Zn alloys [34]. Accordingly, more pinned dislocations with a homogenization distribution can be formed upon the increase of Si content [27]. As a result, it can be proposed that more heterogeneous nucleation sites can be provided as Si content increases, and the corresponding number density of precipitates (β'') in the peak-aged alloys with 2% PD also increases as Si content increases (Fig. 7b, e, h).

However, in the T6 state, the number density of precipitates in the alloys with 8%PD is lower than that of in the alloys with 2%PD, and gradually decreases as Si content increases. There are two main reasons to explain this phenomenon. First, the heterogeneous nucleation rate further increases with the increased dislocations, corresponding to a lower homogeneous nucleation rate in the matrix of no dislocation due to the limited concentration of solute atoms. Second, the homogeneous nucleation rate in the matrix of alloy A is maintained during the isothermal aging process due to the inhomogeneous distribution and low density of dislocations in Mg-rich alloys (alloy A). Meanwhile, precipitates formed along dislocations can rapidly grow and coarsen due to the higher diffusion rate of solute atoms assisted by dislocations. As a result, the average length of needle precipitates increases with increasing pre-deformation ratio. Additionally, based on the HRTEM analysis, the variation of pre-deformation and Si content has little effect on the types of precipitates of Al–Mg–Si–Cu–Zn alloys in the T6 state [26].

Overall, the intragranular precipitation behavior assisted by homogeneous/heterogeneous nucleation can be mainly manifested in the following three aspects: (1) the nucleation of precipitates on dislocations and in the matrix of no dislocations precipitation is complementary; (2) all the precipitates formed along dislocations are still mainly needle-like along the $< 100 >$ Al direction, but the average length of precipitates can be increased while the diameter can be decreased by pre-deformation treatment; (3) the critical growth size of solute clusters can be reduced by pre-deformation, thus promoting the homogeneous nucleation rate in the matrix of no dislocations.

Intergranular precipitation behavior of Al–Mg–xSi–Cu–Zn alloys

The evolution of GBPs and the formation of PFZs are associated well with the intragranular precipitation behavior, which is greatly influenced by the synergistic effect of homogeneous/heterogeneous nucleation. Because excess Si content is prone to segregate at grain boundaries, the nucleation rate of Mg-Si precipitates at grain boundaries can be enhanced. Meanwhile, Si content can also promote the nucleation of precipitates inside the grain [41, 60], leading to an increase in the number density of GBPs and an increase in the widths of PFZs in the undeformed alloys upon the increase of Si content [9, 10].

With the introduction of dislocations, the intergranular precipitate behavior changes significantly. On the one hand, our previous study [27] has shown that the precipitates along dislocations easily nucleate and grow due to the segregation of Mg and Si atoms, but Zn atoms are rejected from the precipitates upon growth with the highest diffusion coefficient. Consequently, the interaction force between Mg and Zn atoms may be stronger in the matrix of no dislocations, and Mg–Zn precipitates can be formed in the

matrix of no dislocations which can promote the formation of Mg–Si–Cu–Zn complex solute clusters or precipitates. As a result, the segregation of Zn atoms at grain boundaries can be suppressed. Therefore, the GBPs of the undeformed alloy are mainly composed of Mg, Si, Cu, and Zn solute atoms, while the GBPs of the pre-deformed alloy are mainly composed of Mg and Si solute atoms (Fig. 10). On the other hand, dislocations were entangled and stored at grain boundaries with a high pre-deformation ratio, which can promote the formation of coarse Mg-Si metastable precipitates at the grain boundaries. Furthermore, more dislocations with a uniform distribution can be formed as Si content increases, so the intragranular precipitation behavior can be greatly enhanced by coupling Si content and pre-deformation treatment. In addition, dislocation-assisted pipe diffusion easily leads to the segregation of solute atoms (Mg, Si, Cu, and Zn) along dislocations, thus limiting the segregation of solute atoms at grain boundaries. Accordingly, the segregation of solute atoms at the grain boundaries may be suppressed, thus inhibiting the formation of GBPs, which ultimately results in a low number density of GBPs and a narrow width of PFZs in the pre-deformed alloy (Figs. 9 and 11). In addition, the formation of Cu-rich film or Zn-rich film along grain boundaries can also be inhibited by pre-deformation treatment (Fig. 10). However, at the low pre-deformation ratio (2%), the rapid nucleation rate of intragranular precipitates assisted by pre-deformation instead promotes the segregation of excess Mg or Si content at grain boundaries due to the low density of dislocations. Accordingly, for Mg-rich alloy A with 2% PD, a continuous distribution of the Mg–Si phase is formed which is consistent with the research on Mg-rich alloys (Fig. 9b) [61]. For Si-rich alloy C with 2% PD, excess Si contents are prone to segregate at grain boundaries and coarse Si particles can be formed at grain boundaries (Fig. 9h).

In short, heterogeneous precipitates can preferentially precipitate along dislocations due to the enhanced diffusion rate of solute atoms [43–45]. Meanwhile, dislocations can also promote the nucleate and growth rate of precipitates in the matrix of no dislocation during the isothermal aging process with the enhanced interaction force between Mg and Zn, thereby affecting the solute partitioning at grain boundaries. Moreover, the segregation of solute atoms at grain boundaries can be suppressed. Consequently, the intragranular precipitation behavior can be regulated by dislocations, correspondingly decorating the intergranular precipitation behavior, and finally leading to a significant decrease in the number density of precipitates at grain boundaries and the widths of PFZs.

Synergy of intragranular/intergranular precipitations on IGC susceptibility

The IGC susceptibility of Al–Mg–Si–Cu–Zn alloys greatly depends on the formation of continuous electrochemical micro-couplings consisting of GBPs and PFZs along grain boundaries. To eliminate the IGC susceptibility caused by continuous micro-couplings, there are two main ways: (i) breaking up the continuity of the GBPs or suppressing the formation of the GBPs and (ii) eliminating or reducing the PFZs [15, 33, 62–64]. In the present study, combining Si content with pre-deformation can greatly change both GBPs and PFZs by the synergy of the intragranular and intergranular precipitation behaviors. To clearly describe the evolution of the intragranular and intergranular precipitates, Fig. 12 gives the schematic diagram of the microstructure for the peak-aged alloys with different pre-deformation ratios.

Based on the concept of electrochemical micro-couples, the change in IGC susceptibility of undeformed alloys must be related to the effect of Si content on the continuity of the electrochemical micro-couples along the grain boundaries. The continuity of the GBPs and PFZs increases with increasing Si content due to the enhanced nucleation rate of precipitates by Si content at grain boundaries (Fig. 12a1–c1), which is in agreement with those reported by other studies [11, 65, 66]. According to the EDS analysis, the GBPs are mainly composed of Zn-containing Mg-Si and Si phases, which are commonly present in 6xxx series Al–Mg–Si alloys (Fig. 10) [11, 20, 67]. Consequently, the continuous micro-coupling of undeformed alloys consists of GBPs and PFZs. However, Si particles can be formed at grain boundaries when the Mg/Si atomic ratio is less than 1.04 (alloys B and C). It is suggested that pure Si particles are an ineffective cathode because they are covered by an insulating layer of SiO_2 in contact with water [4, 16, 68, 69]. Accordingly, the E_{corr} value first increases slightly and then decreases, but the I_{corr} value increases upon increases in Si content due to the increased continuity of GBPs

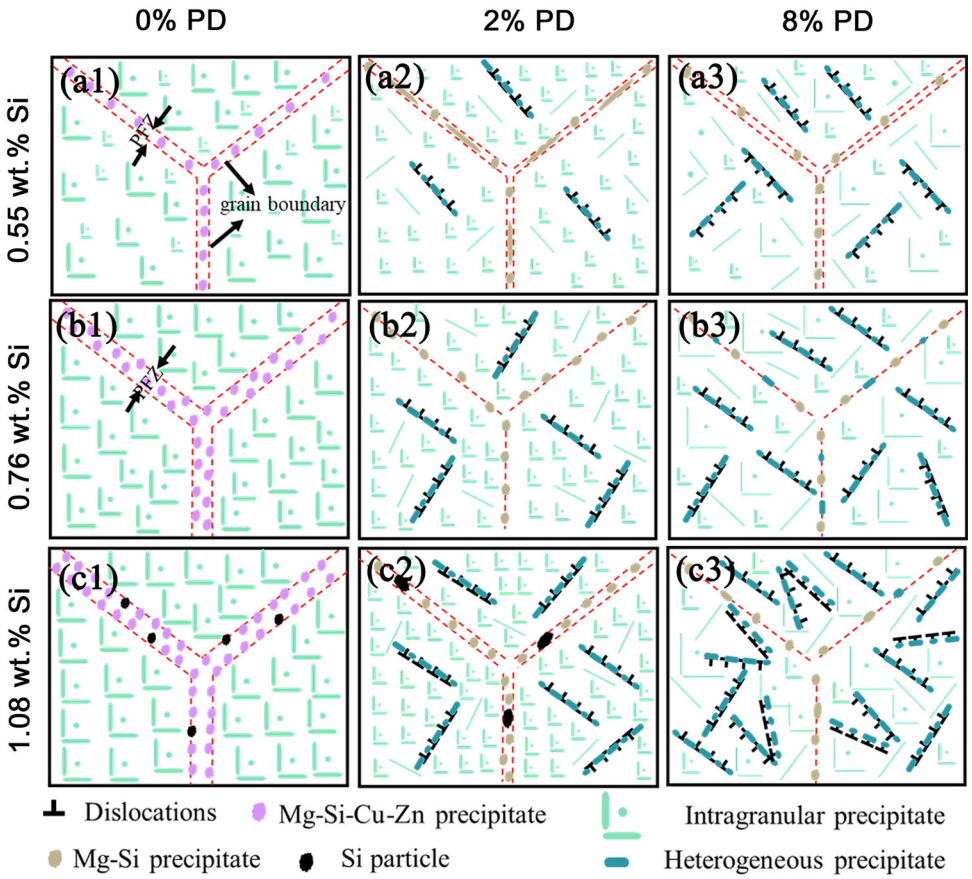

Figure 12 Schematic diagram of the microstructure in the three Al–Mg–Si–Cu–Zn alloys with different pre-deformation (PD) ratios in the peak aged state.

(Fig. 6 and Table 2). As a result, the IGC susceptibility of the undeformed alloys increases as Si content and then remains constant in the excess Si content alloys (Figs. 4 and 5).

When the pre-aged alloys are subjected to pre-deformation treatment, the intragranular and intergranular precipitation behavior has been greatly changed, where there is a substantial decrease in GBPs and PFZs, resulting in a higher IGC resistance, except for alloy A with 2%PD. For alloy A with excess Mg, the continuous GBPs first increase and then decrease accompanied by a decrease in PFZs, when the pre-deformation gradually increases to 8% (Fig. 12 a1–a3). Accordingly, the continuous micro-coupling of deformed alloy A also consists of GBPs and PFZs. The higher IGC susceptibility of alloy A with 2% PD is mainly attributed to the more continuous GBPs with a higher I_{corr} value. In addition, excess Mg atoms preferentially segregate along the grain boundaries, which is detrimental to the IGC resistance. Some studies have demonstrated that Mg segregations along grain boundaries can promote intergranular corrosion in aluminum alloys due to the preferential dissolution of Mg at the electrochemical micro-couples [61]. With further increases in pre-deformation ratio, whether GBPs or PFZs decrease and the segregation of Mg is suppressed, leading to the improvement in the IGC resistance in alloy A.

For alloy B with different pre-deformation ratios, the PFZs have almost been eliminated, and the continuity of stable GBPs decreased (Fig. 12b1–b3). Therefore, the continuous micro-coupling of deformed alloy B is considered to consist of GBPs and Al matrix. Furthermore, many metastable Mg–Si phases gradually nucleate and grow along grain boundaries as a pre-deformation ratio increases to 8%. Although stable Mg–Si particles are beneficial for improving the corrosion resistance compared to alloys with coherent Mg–Si precipitates, the nucleation rate of coherent Mg–Si precipitates has been limited. As a result, the IGC susceptibility of alloy B decreases first and then increases slightly when the pre-deformation ratio increases gradually to 8%, which is consistent with the change in the I_{corr} value.

Furthermore, the continuous GBPs and PFZs show a substantial decrease in Si-rich alloy C when the pre-deformation gradually increases to 8% (Fig. 12c3). In addition, some Si particles formed along grain boundaries due to the segregation of excess Si atoms (Fig. 12c2). The corrosion potentials of the Al matrix, Si, and Mg_2Si arranged in decreasing order for the Al–Mg–Si alloy are as follows: Si > Al matrix > Mg_2Si in 3.5 wt% NaCl solution [10, 15]. Therefore, corrosion preferentially develops on the surface of Mg_2Si particles. Although there is substantial evidence to suggest that Si is an ineffective cathode in aluminum alloys, precipitated elemental Si on grain boundaries was claimed to act as local cathodic sites in alloys containing excess Si. However, with dissolution, the Mg_2Si particles become enriched with Si because of the preferential dissolution of Mg from the Mg_2Si particles [10, 65]. In this way, the Si-enriched phases serve as cathodes to induce IGC. Some literature has shown that preferential segregation of Si at the grain boundaries increases the IGC susceptibility of Al–Mg–Si alloys [10]. Here, although Si particles formed along grain boundaries, Mg–Si particles were distributed more discontinuously with a substantial decrease in density by pre-deformation. Correspondingly, the I_{corr} value decreased, and the IGC resistance of deformed alloy C was enhanced. Hereafter, with further increasing pre-deformation, the PFZs were eliminated with the more discontinuous distribution of GBPs. Finally, it is difficult to form corrosion micro-couplings between the alloy matrix and GBPs. Accordingly, it can be concluded that the IGC susceptibility of Al–Mg–Si–Cu–Zn alloys can be regulated by coupling pre-deformation and Si content.

Conclusions

In this study, the intragranular and intergranular precipitation behavior of Al–Mg–Si–Cu–Zn alloys has been systematically investigated via coupling pre-deformation and Si content. Subsequently, the mechanism between precipitation microstructure and the strength, ductility, and IGC susceptibility of the peak-aged alloys was deeply analyzed. The following conclusions can be drawn:

(1) The strength and ductility of the peak-aged Al–Mg–Si–Cu–Zn alloys increase, but intergranular corrosion resistance first decreases and then remain stable as Si content increases. With the introduction of dislocations by pre-deformation, the age-hardening response and intergranular corrosion resistance of Al–Mg–Si–Cu–Zn alloys have been largely improved without losing their strength and ductility.

(2) The intragranular precipitation behavior in the Al–Mg–Si–Cu–Zn alloys is strongly associated with the change in pre-deformation ratio and Si content. First, precipitates (GP zones, β'' phase and pre-Q' phase) can preferentially nucleate and grow along dislocations induced by pre-deformation, while the nucleation rate of precipitates in the matrix of no dislocations can also be enhanced. Second, the average length of needle precipitates increases with increasing pre-deformation ratio due to the higher diffusion rate of solute atoms assisted by dislocations. Accordingly, the age-hardening response can be enhanced by pre-deformation treatment. In addition, in the pre-deformed alloys, the average length of the needle-like precipitates increases while the diameter decreases due to the mutually exclusive effect of nucleation rate and growth rate of the precipitates.

(3) The intergranular precipitation behavior is associated well with Si content and pre-deformation ratios. In general, the continuity GBPs and width of PFZs decrease after appropriate pre-deformation treatment, because the segregation of solute atoms at the grain boundaries can be suppressed and the nucleation rate of intragranular precipitates can be enhanced by pre-deformation treatment. Especially, the segregation of Cu atoms or Zn atoms at grain boundaries can be suppressed due to the enhanced interaction force between Mg and Zn atoms, so the formation of Cu-rich film or Zn-rich film along grain boundaries can also be inhibited by pre-deformation treatment. However, excess Si or Mg content is instead preferentially segregated along grain boundaries with the low density of dislocations, thus affecting the nucleation rate of the GBPs and ultimately affecting the IGC resistance. The related mechanisms have been discussed in this paper.

Funding

This work was supported by the National Key Research and Development Program of China (Nos. 2021YFE0115900, 2016YFB0300801), National Natural Science Foundation of China (Nos. 51871029,

51571023 and 51301016), Government Guided Program-Intergovernmental Bilateral Innovation Cooperation Project (No. BZ2019019), the Opening Project of State Key Lab of Advanced Metals and Materials (Nos. 2020-ZD02, 2022-Z03) and Industry-University Cooperation Collaborative Education Project (Nos. 202102437001, 202102437002).

Declarations

Conflict of interest The authors declare that they have no conflict of interest.

References

[1] Werinos M, Antrekowitsch H, Ebner T et al (2016) Design strategy for controlled natural aging in Al–Mg–Si alloys. Acta Mater 118:296–305. https://doi.org/10.1016/j.actamat.2016.07.048

[2] Sun W, Zhu Y, Marceau R et al (2019) Precipitation strengthening of aluminum alloys by room-temperature cyclic plasticity. Science 363:972–975. https://doi.org/10.1126/science.aav7086

[3] Svenningsen G, Larsen MH, Nordlien JH, Nisancioglu K (2006) Effect of thermomechanical history on intergranular corrosion of extruded AlMgSi(Cu) model alloy. Corros Sci 48:3969–3987. https://doi.org/10.1016/j.corsci.2006.03.018

[4] Svenningsen G, Larsen MH, Walmsley JC, Nordlien JH, Nisancioglu K (2006) Effect of artificial aging on intergranular corrosion of extruded AlMgSi alloy with small Cu content. Corros Sci 48:1528–1543. https://doi.org/10.1016/j.corsci.2005.05.045

[5] Li H, Zhao P, Wang Z et al (2016) The intergranular corrosion susceptibility of a heavily overaged Al-Mg-Si-Cu alloy. Corros Sci 107:113–122. https://doi.org/10.1016/j.corsci.2016.02.025

[6] El-Menshawy K, El-Sayed A-WA, El-Bedawy ME, Ahmed HA, El-Raghy SM (2012) Effect of aging time at low aging temperatures on the corrosion of aluminum alloy 6061. Corros Sci 54:167–173. https://doi.org/10.1016/j.corsci.2011.09.011

[7] Sekhar AP, Das D (2019) Corrosion behavior of under-, peak-, and over-aged 6063 alloy: A comparative study. Mater Corros 70:2052–2063. https://doi.org/10.1002/maco.201910961

[8] Li H, Qingzhong M, Wang Z et al (2014) Simultaneously enhancing the tensile properties and intergranular corrosion resistance of Al–Mg–Si–Cu alloys by a thermo-mechanical treatment. Mater Sci Eng A 617:165–174. https://doi.org/10.1016/j.msea.2014.08.045

[9] Kairy SK, Rometsch PA, Diao K, Nie JF, Davies CHJ, Birbilis N (2016) Exploring the electrochemistry of 6xxx series aluminium alloys as a function of Si to Mg ratio, Cu content, ageing conditions and microstructure. Electrochim Acta 190:92–103. https://doi.org/10.1016/j.electacta.2015.12.098

[10] Larsen MH, Walmsley JC, Lunder O, Nisancioglu K (2010) Effect of excess silicon and small copper content on intergranular corrosion of 6000-series aluminum alloys. J Electrochem Soc 157:C61. https://doi.org/10.1149/1.3261804

[11] Zou Y, Liu Q, Jia Z, Xing Y, Ding L, Wang X (2017) The intergranular corrosion behavior of 6000-series alloys with different Mg/Si and Cu content. Appl Surf Sci 405:489–496. https://doi.org/10.1016/j.apsusc.2017.02.045

[12] Zhu L, Guo M, Zhang J (2021) The multi-scale Si-containing phases-assisted improvement in the microstructure and mechanical properties of Al–Mg-xSi-Cu-Zn alloys. Mater Sci Eng A 826:142013. https://doi.org/10.1016/j.msea.2021.142013

[13] Li Z, Zhao P, Jia Z, Liu Z, Xie Z (2019) Effects of Mg and Si contents on the microstructure and mechanical properties of AA6014 alloys in T4P and T6P temper. Mater Sci Eng A 740–741:187–200. https://doi.org/10.1016/j.msea.2018.10.043

[14] Buchanan K, Colas K, Ribis J, Lopez A, Garnier J (2017) Analysis of the metastable precipitates in peak-hardness aged Al-Mg-Si(-Cu) alloys with differing Si contents. Acta Mater 132:209–221. https://doi.org/10.1016/j.actamat.2017.04.037

[15] Zeng F, Wei Z, Li J et al (2011) Corrosion mechanism associated with Mg2Si and Si particles in Al–Mg–Si alloys. Trans Nonferrous Met Soc China 21:2559–2567. https://doi.org/10.1016/s1003-6326(11)61092-3

[16] Liang WJ, Rometsch PA, Cao LF, Birbilis N (2013) General aspects related to the corrosion of 6xxx series aluminium alloys: exploring the influence of Mg/Si ratio and Cu. Corros Sci 76:119–128. https://doi.org/10.1016/j.corsci.2013.06.035

[17] Saito T, Wenner S, Osmundsen E et al (2014) The effect of Zn on precipitation in Al–Mg–Si alloys. Philos Mag 94:2410–2425. https://doi.org/10.1080/14786435.2014.913819

[18] Zhu S, Li Z, Yan L et al (2018) Effects of Zn addition on the age hardening behavior and precipitation evolution of an Al-Mg-Si-Cu alloy. Mater Charact 145:258–267. https://doi.org/10.1016/j.matchar.2018.08.051

[19] Guo MX, Li GJ, Zhang YD et al (2019) Influence of Zn on the distribution and composition of heterogeneous solute-rich features in peak aged Al-Mg-Si-Cu alloys. Scr Mater 159:5–8. https://doi.org/10.1016/j.scriptamat.2018.09.004

[20] Guo MX, Du JQ, Zheng CH, Zhang JS, Zhuang LZ (2019) Influence of Zn contents on precipitation and corrosion of Al-Mg-Si-Cu-Zn alloys for automotive applications. J Alloy Compd 778:256–270. https://doi.org/10.1016/j.jallcom.2018.11.146

[21] Lutz A, Malet L, Dille J et al (2019) Effect of Zn on the grain boundary precipitates and resulting alkaline etching of recycled Al-Mg-Si-Cu alloys. J Alloy Compd 794:435–442. https://doi.org/10.1016/j.jallcom.2019.04.259

[22] Wang Z, Li H, Miao F et al (2014) Improving the intergranular corrosion resistance of Al–Mg–Si–Cu alloys without strength loss by a two-step aging treatment. Mater Sci Eng A 590:267–273. https://doi.org/10.1016/j.msea.2013.10.001

[23] Xu X, Deng Y, Pan Q, Guo X (2021) Enhancing the intergranular corrosion resistance of the Al–Mg–Si alloy with low Zn content by the interrupted aging treatment. Metall Mater Trans A 52:4907–4921. https://doi.org/10.1007/s11661-021-06433-z

[24] Dumitraschkewitz P, Uggowitzer PJ, Gerstl SSA, Löffler JF, Pogatscher S (2019) Size-dependent diffusion controls natural aging in aluminium alloys. Nat Commun 10:4746. https://doi.org/10.1038/s41467-019-12762-w

[25] Yang M, Liu S, He X et al (2017) Effect of stamping deformation on microstructure and properties evolution of an Al–Mg–Si–Cu alloy for automotive panels. J Mater Sci 52:5569–5581. https://doi.org/10.1007/s10853-016-0278-9

[26] Lai YX, Fan W, Yin MJ, Wu CL, Chen JH (2020) Structures and formation mechanisms of dislocation-induced precipitates in relation to the age-hardening responses of Al-Mg-Si alloys. J Mater Sci Technol 41:127–138. https://doi.org/10.1016/j.jmst.2019.11.001

[27] Zhu L, Guo M, Wu Y, Zhu H, Zhang J (2022) Ultra-fast bake-hardening response of Al-Mg-Si-Cu-Zn alloys with the assistance of heterogeneous nucleation. J Mater Res Technol-JMRT 18:1009–1016. https://doi.org/10.1016/j.jmrt.2022.03.018

[28] Xu LY, Cheng YF (2012) Corrosion of X100 pipeline steel under plastic strain in a neutral pH bicarbonate solution. Corros Sci 64:145–152. https://doi.org/10.1016/j.corsci.2012.07.012

[29] Peguet L, Malki B, Baroux B (2007) Influence of cold working on the pitting corrosion resistance of stainless steels. Corros Sci 49:1933–1948. https://doi.org/10.1016/j.corsci.2006.08.021

[30] Beura VK, Kale C, Srinivasan S, Williams CL, Solanki KN (2020) Corrosion behavior of a dynamically deformed Al–Mg alloy. Electrochim Acta 354:136695. https://doi.org/10.1016/j.electacta.2020.136695

[31] Fu Y, Wu X, Han E, Ke W, Yang K, Jiang Z (2008) Influence of cold work on pitting corrosion behavior of a high nitrogen stainless steel. J Electrochem Soc 155:C455. https://doi.org/10.1149/1.2939213

[32] Zhang X, Zhou X, Cai G et al (2018) The influence of stored energy on grain boundary chemistry and intergranular corrosion development in AA2024-T3 alloy. Materials (Basel) 11:2299. https://doi.org/10.3390/ma11112299

[33] Zhou X, Luo C, Ma Y et al (2013) Grain-stored energy and the propagation of intergranular corrosion in AA2xxx aluminium alloys. Surf Interface Anal 45:1543–1547. https://doi.org/10.1002/sia.5218

[34] Zhu L, Guo M, Zhang J (2022) Effect of silicon content on nucleation and growth of multiscale precipitates in Al–Mg–Si–Cu–Zn alloys for different aging paths. Mater Sci Eng A 841:143016. https://doi.org/10.1016/j.msea.2022.143016

[35] Maeda T, Kaneko K, Namba T et al (2018) Structural and compositional study of precipitates in under-aged Cu-added Al-Mg-Si alloy. Sci Rep 8:16629. https://doi.org/10.1038/s41598-018-35134-8

[36] Hasting HS, Frøseth AG, Andersen SJ et al (2009) Composition of β″ precipitates in Al-Mg-Si alloys by atom probe tomography and first principles calculations. J Appl Phys 106:123527. https://doi.org/10.1063/1.3269714

[37] Ninive PH, Strandlie A, Gulbrandsen-Dahl S et al (2014) Detailed atomistic insight into the β″ phase in Al-Mg-Si alloys. Acta Mater 69:126–134. https://doi.org/10.1016/j.actamat.2014.01.052

[38] Myhr OR, Grong O, Fjaer HG, Marioara CD (2004) Modelling of the microstructure and strength evolution in Al-Mg-Si alloys during multistage thermal processing. Acta Mater 52:4997–5008. https://doi.org/10.1016/j.actamat.2004.07.002

[39] Wang W, Pan Q, Wang X et al (2020) Non-isothermal aging: a heat treatment method that simultaneously improves the mechanical properties and corrosion resistance of ultra-high strength Al-Zn-Mg-Cu alloy. J Alloy Compd 845:156286. https://doi.org/10.1016/j.jallcom.2020.156286

[40] Wang Z, Chen P, Li H, Fang B, Song R, Zheng Z (2017) The intergranular corrosion susceptibility of 2024 Al alloy during re–ageing after solution treating and cold–rolling. Corros Sci 114:156–168. https://doi.org/10.1016/j.corsci.2016.11.013

[41] Gupta AK, Lloyd DJ, Court SA (2001) Precipitation hardening in Al-Mg-Si alloys with and without excess Si. Mater Sci Eng A 316:11–17. https://doi.org/10.1016/S0921-5093(01)01247-3

[42] Guo MX, Zhang YD, Li GJ et al (2019) Solute clustering in Al-Mg-Si-Cu-(Zn) alloys during aging. J Alloy Compd 774:347–363. https://doi.org/10.1016/j.jallcom.2018.09.309

[43] Legros M, Dehm G, Arzt E, Balk TJ (2008) Observation of giant diffusivity along dislocation cores. Science 319:1646–1649. https://doi.org/10.1126/science.1151771

[44] Jiang S, Wang H, Wu Y et al (2017) Ultrastrong steel via minimal lattice misfit and high-density nanoprecipitation. Nature 544:460–464. https://doi.org/10.1038/nature22032

[45] Li X, Wei Y, Lu L, Lu K, Gao H (2010) Dislocation nucleation governed softening and maximum strength in nano-twinned metals. Nature 464:877–880. https://doi.org/10.1038/nature08929

[46] He BB, Hu B, Yen HW et al (2017) High dislocation density-induced large ductility in deformed and partitioned steels. Science 357:1029–1032. https://doi.org/10.1126/science.aan0177

[47] Aruga Y, Kozuka M, Takaki Y, Sato T (2016) Effects of natural aging after pre-aging on clustering and bake-hardening behavior in an Al–Mg–Si alloy. Scr Mater 116:82–86. https://doi.org/10.1016/j.scriptamat.2016.01.019

[48] Weng Y, Jia Z, Ding L, Liu M, Wu X, Liu Q (2018) Combined effect of pre-aging and Ag/Cu addition on the natural aging and bake hardening in Al-Mg-Si alloys. Prog Nat Sci 28:363–370. https://doi.org/10.1016/j.pnsc.2018.04.007

[49] Cao L, Rometsch PA, Couper MJ (2013) Effect of pre-ageing and natural ageing on the paint bake response of alloy AA6181A. Mater Sci Eng A 571:77–82. https://doi.org/10.1016/j.msea.2013.01.065

[50] De Geuser F, Lefebvre W, Blavette D (2006) 3D atom probe study of solute atoms clustering during natural ageing and pre-ageing of an Al-Mg-Si alloy. Philos Mag Lett 86:227–234. https://doi.org/10.1080/09500830600643270

[51] Ding LP, He Y, Wen Z, Zhao PZ, Jia ZH, Liu Q (2015) Optimization of the pre-aging treatment for an AA6022 alloy at various temperatures and holding times. J Alloy Compd 647:238–244. https://doi.org/10.1016/j.jallcom.2015.05.188

[52] Stemper L, Tunes MA, Dumitraschkewitz P et al (2021) Giant hardening response in AlMgZn(Cu) alloys. Acta Mater 206:116617. https://doi.org/10.1016/j.actamat.2020.116617

[53] Noronha SJ, Farkas D (2002) Dislocation pinning effects on fracture behavior: atomistic and dislocation dynamics simulations. Phys Rev B 66:132103. https://doi.org/10.1103/PhysRevB.66.132103

[54] Singh CV, Mateos AJ, Warner DH (2011) Atomistic simulations of dislocation–precipitate interactions emphasize importance of cross-slip. Scr Mater 64:398–401. https://doi.org/10.1016/j.scriptamat.2010.10.041

[55] Teichmann K, Marioara CD, Andersen SJ, Marthinsen K (2013) TEM study of β′ precipitate interaction mechanisms with dislocations and β′ interfaces with the aluminium matrix in Al–Mg–Si alloys. Mater Charact 75:1–7. https://doi.org/10.1016/j.matchar.2012.10.003

[56] Kacher J, Eftink BP, Cui B, Robertson IM (2014) Dislocation interactions with grain boundaries. Curr Opin Solid State Mater Sci 18:227–243. https://doi.org/10.1016/j.cossms.2014.05.004

[57] Masuda H, Sato E (2020) Diffusional and dislocation accommodation mechanisms in superplastic materials. Acta Mater 197:235–252. https://doi.org/10.1016/j.actamat.2020.07.042

[58] Wang CY, Cepeda-Jiménez CM, Pérez-Prado MT (2020) Dislocation-particle interactions in magnesium alloys. Acta Mater 194:190–206. https://doi.org/10.1016/j.actamat.2020.04.055

[59] Fan H, Wang Q, El-Awady JA, Raabe D, Zaiser M (2021) Strain rate dependency of dislocation plasticity. Nat Commun 12:1–11. https://doi.org/10.1038/s41467-021-21939-1

[60] Maruyama N, Uemori R, Hashimoto N, Saga M, Kikuchi M (1997) Effect of silicon addition on the composition and structure of fine-scale precipitates in Al-Mg-Si alloys. Scr Mater 36:89–93. https://doi.org/10.1016/S1359-6462(96)00358-2

[61] Ding Y, Gao K, Huang H et al (2019) Nucleation and evolution of β phase and corresponding intergranular corrosion transition at 100–230 °C in 5083 alloy containing Er and Zr. Mater Des 174:107778. https://doi.org/10.1016/j.matdes.2019.107778

[62] Eckermann F, Suter T, Uggowitzer PJ, Afseth A, Schmutz P (2008) The influence of MgSi particle reactivity and dissolution processes on corrosion in Al–Mg–Si alloys. Electrochim Acta 54:844–855. https://doi.org/10.1016/j.electacta.2008.05.078

[63] Larsen MH, Walmsley JC, Lunder O, Mathiesen RH, Nisancioglu K (2008) Intergranular corrosion of copper-containing AA6xxx AlMgSi aluminum alloys. J Electrochem Soc 155:C550. https://doi.org/10.1149/1.2976774

[64] Zander D, Schnatterer C, Altenbach C, Chaineux V (2015) Microstructural impact on intergranular corrosion and the mechanical properties of industrial drawn 6056 aluminum wires. Mater Des 83:49–59. https://doi.org/10.1016/j.matdes.2015.05.079

[65] Zheng Y, Luo B, Bai Z, Wang J, Yin Y (2017) Study of the precipitation hardening behaviour and intergranular corrosion of Al-Mg-Si alloys with differing Si contents. Metals 7:387. https://doi.org/10.3390/met7100387

[66] Kairy SK, Rometsch PA, Davies CHJ, Birbilis N (2017) On the intergranular corrosion and hardness evolution of 6xxx series Al alloys as a function of Si: Mg ratio, Cu content, and aging condition. Corros 73:1280–1295. https://doi.org/10.5006/2506

[67] Zhang XX, Zhou XR, Nilsson JO (2019) Corrosion behaviour of AA6082 Al-Mg-Si alloy extrusion: the influence of

quench cooling rate. Corros Sci 150:100–109. https://doi.org/10.1016/j.corsci.2019.01.030

[68] Serdechnova M, Volovitch P, Brisset F, Ogle K (2014) On the cathodic dissolution of Al and Al alloys. Electrochim Acta 124:9–16. https://doi.org/10.1016/j.electacta.2013.09.145

[69] Zheng Q, Wu J, Jiang H, Zhang L, Zhao J, He J (2021) Effect of micro-alloying element La on corrosion behavior of Al–Mg–Si alloys. Corros Sci 179:109113. https://doi.org/10.1016/j.corsci.2020.109113